



저작자표시-비영리-변경금지 2.0 대한민국

이용자는 아래의 조건을 따르는 경우에 한하여 자유롭게

- 이 저작물을 복제, 배포, 전송, 전시, 공연 및 방송할 수 있습니다.

다음과 같은 조건을 따라야 합니다:



저작자표시. 귀하는 원저작자를 표시하여야 합니다.



비영리. 귀하는 이 저작물을 영리 목적으로 이용할 수 없습니다.



변경금지. 귀하는 이 저작물을 개작, 변형 또는 가공할 수 없습니다.

- 귀하는, 이 저작물의 재이용이나 배포의 경우, 이 저작물에 적용된 이용허락조건을 명확하게 나타내어야 합니다.
- 저작권자로부터 별도의 허가를 받으면 이러한 조건들은 적용되지 않습니다.

저작권법에 따른 이용자의 권리는 위의 내용에 의하여 영향을 받지 않습니다.

이것은 [이용허락규약\(Legal Code\)](#)을 이해하기 쉽게 요약한 것입니다.

[Disclaimer](#)

공학석사 학위논문

Numerical Study on Turbulent
Flow and Flame Characteristics of
Low-Swirl Combustor Depending
on Turbulence Generating Plate

난류생성판에 따른 저선회 연소기의 난류 및 연소
특성에 관한 수치적 연구

2023년 02월

서울대학교 대학원

협동과정 우주시스템전공

전 병 주

Numerical Study on Turbulent
Flow and Flame Characteristics of
Low-Swirl Combustor Depending
on Turbulence Generating Plate

난류생성판에 따른 저선회 연소기의 난류 및 연소
특성에 관한 수치적 연구

지도 교수 이 복 직

이 논문을 공학석사 학위논문으로 제출함
2022년 12월

서울대학교 대학원
협동과정 우주시스템전공
전 병 주

전병주의 공학석사 학위논문을 인준함
2022년 12월

위 원 장 _____ (인)

부위원장 _____ (인)

위 원 _____ (인)

Abstract

**Numerical Study on Turbulent Flow and
Flame Characteristics of Low-Swirl
Combustor Depending on Turbulence
Generating Plate**

Byoungjoo Chun

Interdisciplinary Program in Space Systems

The Graduate School

Seoul National University

Low-swirl flame is formed when there is insufficient angular momentum to break down the vortex, resulting in recirculation. Instead, as it leaves the confines of the combustion chamber, the flow stream diverges. A numerical study of a real scale low-swirl combustor was performed with different types of turbulence generating plates for different blockage ratios and different numbers of fractal pattern iterations. In the present study, the pressure-based Navier-Stokes equations were solved using a three-dimensional large eddy simulation with dynamic Smagorinsky for a premixed methane/air intake at an equivalence ratio of 0.49 and ambient pressure. Sub-grid based adaptive mesh refinement method was used to obtain a refined grid in flow regions of interest. The maximum error of the swirl number between numerical results and experimental data was less than 0.9%. After the simulation was validated, the effect of four distinct fractal geometries on turbulence intensity as the primary

factor for achieving more complete combustion was evaluated. In the nonreacting mode, the fractal with a 73% blockage ratio and four iteration levels was the best case for increasing the turbulence intensity, flow residence time, vorticity, and velocity gradient. While for the reacting mode, the fractal with a 73% blockage ratio and three iteration levels was the worst case. In addition, we examined the flame front and reaction zone for these two cases in the reacting mode. The optimal case demonstrates improved combustion efficiency, resulting in an increase in the hydroxide (OH) radical and a decrease in nitric oxide (NO) emission gas.

Keywords: Low-swirl combustion, Computational fluid dynamics (CFD), Large-eddy simulation (LES), Adaptive mesh refinement (AMR), Turbulence generating plate, Fractal geometry

Student Number: 2021-26314

Contents

1	Introduction	1
2	Numerical Methods	9
2.1	Turbulence Model.....	9
2.2	Combustion Model	12
2.3	Computational Domain.....	13
2.4	Adaptive Mesh Refinement	19
3	Validation Study	21
3.1	Swirl Number	21
4	Results and Discussion	23
4.1	Nonreacting Mode	23
4.1.1	Velocity Field	23
4.1.2	Vorticity Field	29
4.1.3	Streamline.....	31
4.2	Reacting Mode.....	33
4.2.1	Hydroxide (OH) mole fraction.....	33
4.2.2	Formaldehyde (CH ₂ O) mole fraction	35
4.2.3	Hydroperoxyl (HO ₂) mole fraction	37
4.2.4	Emission gas	41
5	Conclusion	43
	Bibliography.....	46
	Abstract in Korean	54

List of Figures

Figure 1.1	High-swirl (left) and low-swirl (right) combustion	2
Figure 2.1	Computational domain of the real scale low-swirl combustor	14
Figure 2.2	Name <i>Z1 – Z5</i> to burner and chamber section	15
Figure 2.3	Definition of the fractal cross pattern [21]	16
Figure 2.4	Definition of circular cropped fractal grid with three iterations [21]	17
Figure 2.5	Four types of turbulence generating plate	18
Figure 2.6	Velocity field with adaptive mesh refinement	20
Figure 3.1	Swirl number comparison between numerical results and experimental data	22
Figure 4.1	The cross section of flow direction deviation through the blocked part of plate (a) and the hole part of plate (b) in Case 1	23
Figure 4.2	Axial velocity distribution at various axial distances perpendicular to the flow	25
Figure 4.3	Flow velocity distribution in Case 3 and Case 4	27
Figure 4.4	Instantaneous vorticity distribution for all cases	30
Figure 4.5	Streamline of average velocity flow fields for all cases ..	32
Figure 5.1	Hydroxide (OH) mole fraction distribution in Case 3 and Case 4	34
Figure 5.2	Formaldehyde (CH ₂ O) mole fraction distribution in Case 3 and Case 4	36
Figure 5.3	Radial variation of the Hydroperoxyl (HO ₂) radical in Case 3 and Case 4	39
Figure 5.4	NO and CO emissions in Case 3 and Case 4	42

List of Tables

Table 2.1	Characteristics of turbulence generating plate	17
Table 2.1	Reaction mechanisms that produce Hydroperoxyl (HO ₂) species [45]	38

Chapter 1. Introduction

The swirling flow have been indispensable to both premixed and non-premixed combustion systems due to their strong beneficial effects on flame stability, combustor performance, and combustion intensity. Gas turbine combustors and industrial systems employed a high-swirl type of burner in which the swirling motion generated by the injector is sufficiently enough to produce a fully developed internal recirculation zone at the entrance of the combustor.

Cheng [1] proposed low-swirl combustion based on the notion of flow propagation. As shown in Fig. 1.1, a low-swirl flame is produced when there is insufficient angular momentum to break down the vortex, resulting in recirculation. The flow diverges as it leaves the boundaries of the combustion chamber. Both swirlers in Fig. 1.1, have outer recirculation zone (ORZ) in front of dump plate, while the inner recirculation zone (IRZ) only occurs near the center body at high-swirl combustion. The concept of low-swirl combustion is fundamentally distinct from the high-swirl theory of typical Dry Low NO_x (DLN) gas turbines, in which powerful toroidal vortexes are the essential flow elements for holding and repeatedly reigniting flames.

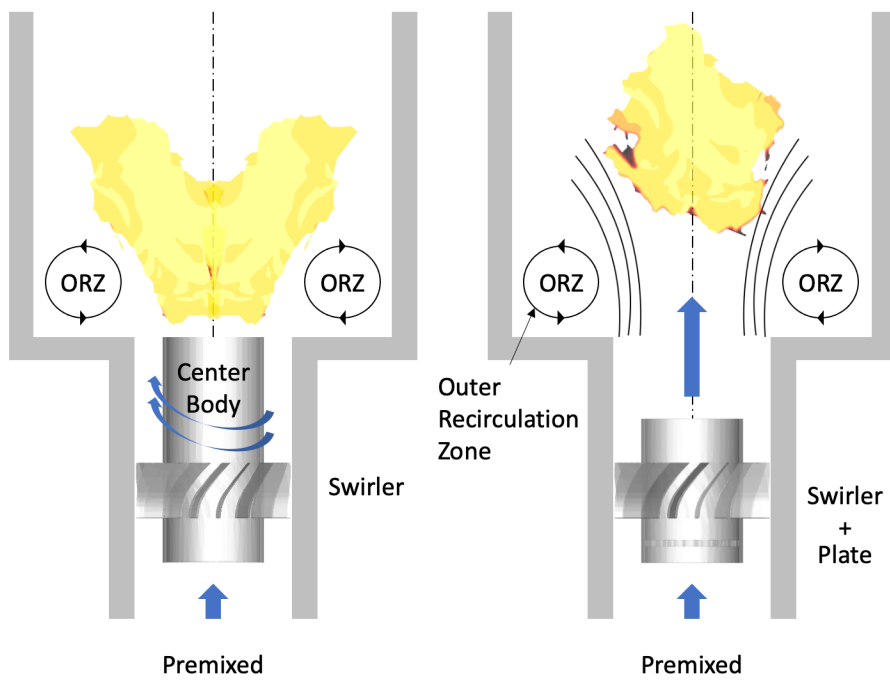


Figure 1.1 High-swirl (left) and low-swirl (right) combustion

The principle of fractal-generated turbulence is utilized in fundamental studies on heat transfer enhancement [2] and flow field features using impinging jets [3], and liquid-phase processes in many industries, including the polymer, fine chemical, pharmaceutical, and biotechnology [4]. Over the past few decades, these devices have been thoroughly examined [5-7], and many of them have been used for studying the development of different turbulence characteristics.

Furthermore, a study on space-filling fractal square grids, hereafter referred to as fractal square grids (FSGs) [8], showed the presence of a nonequilibrium zone in which turbulence properties evolve more diversely than predicted by classical theory. This finding has been validated using regular and biplanar grids [9,10] in conjunction with immediate downstream observations, offering a new perspective to the classical theory of equilibrium turbulence. FSGs are increasingly being used as turbulence generators for enhancing the mixing of fluids and heat transfer [11]. Cafiero et al. [12] observed that both the ability to generate turbulence at multiple scales and the capacity to tune the peak in the turbulence intensity profile are highly desirable for enhancing heat transfer due to the unique characteristics of FSGs. Also, they found an increase in convective heat transfer rates with FSGs and a uniform distribution of convective heat transfer rates with a regular or single square grid. Hoi et al. [13] found that FSGs can be used to produce a more intermittent vorticity field, higher vorticities, and higher turbulence intensities than a regular grid with the same or higher blockage ratio.

Zheng et al. [5] investigated nonequilibrium dissipation scaling in high Reynolds number (Re) turbulence caused by FSGs. They concluded that the highest position of turbulence intensity is not dependent on Reynolds number, but rather on the ratio between the lengths of the largest grid bars in transverse and vertical directions. Goh et al. [14] used FSGs to eliminate the low turbulence level restrictions associated with conventional perforated plate generators, resulting in a shift of Reynolds number from 50-120 to 130-318. In order to simplify the boundary conditions in computational studies, they determined optimal grid configuration settings with an emphasis on minimizing the impact of the flow upstream of the turbulence generators.

In the compressible regime, Es-Sahli et al. [15] discovered the direct interaction of flows with square and fractal-shaped multiscale structures using large-eddy simulations. The results showed that a fractal plate brings disruption of the flow structures and growth in turbulent mixing in the downstream direction. Furthermore, as the Mach number increased, perceptible wake meandering and higher spread rate of the wake in the lateral direction perpendicular to the streamwise-spanwise plane were observed. Cafiero et al. [16] investigated the flow field topology of a turbulent air jet using an FSG. The usage of the grid has been shown to increase the entrainment rate and, consequently, the jet's scalar transfer. Additionally, the effect of the jet external shear layer on the wake shed by the grid bars significantly reduced the downstream of the turbulence production region compared to the documented

behavior of fractal grids under free-shear conditions. In the fractal grid case study, the organization of large coherent structures is also analyzed and discussed. Nedic et al. [17] showed that large-scale fractal porosity reduces spoiler noise while keeping aerodynamic performance the same and the noise caused by recirculation flow could be reduced low-frequency noise. Laizet and Vassilicos [18] showed that fractal grids compared with regular grids can increase scalar transfer by up to an order of magnitude beyond the location of the peak in the turbulence intensity profile. Kim et al. [19] showed that the turbulence intensity of fractal turbulence generators increased by up to 171% and 404% in comparison to the hex-type turbulence generators (HTGs) and mesh-type turbulence generators (MTGs), respectively.

Giannadakis et al. [20] investigated that the interaction of an inner swirling jet and an outer coaxial annular flow influences the statistical mean and turbulence characteristics of shear layers, and that the formation of recirculation bubbles and vortex rings has a significant impact on the development of the flow field. They also figure out the mixing intensity between the swirling vortex and the outer flow. In the turbulent statistics of the azimuthal shear layer, the effect of the swirl generation method and recirculating flow field topology was apparent, as the recirculation bubble and vortex ring formed in it greatly affect the mixing between the two flows. The turbulent statistics of the azimuthal shear layer show the effect of the methods of swirl formation and recirculating flow field topology, as the recirculation bubble and vortex

ring greatly influence the mixing between the two flows.

Another important application of FTGs is in swirl burners because different levels of turbulence [21] and different durations of the mixing of primary and secondary air have different effects on combustion rate [22-24]. Swirl burners with FTGs are beneficial for both premixed and non-premixed combustion in modern turbine systems since they enhance flame stability, combustion intensity, and combustor performance [25-27]. The use of FTGs generates high levels of turbulence at a specific location downstream of the grids, which is typically much further downstream than a normal square grid with the same solidity; the location also relies on the configuration of the grid. It has been shown that using FTGs instead of conventional square or hexagonal grids doubles the turbulent velocity fluctuations and local consumption rates [21]. In general, the results using fractals show that turbulence can be intensified simultaneously on multiple scales, resulting in the formation of an elongated region of intense turbulence behind the fractal object; the turbulence diminishes further downstream.

Zhou [28] compared the flow and flame structures among various swirl combustors. Their findings demonstrated that differences in the geometrical configuration caused the instantaneous vortices structure and temperature distribution. Soulopoulos et al. [29] showed a distinction between the flame behavior of a fractal grid and a standard square mesh grid with the same effective mesh size and solidity as the fractal grid. At

a given distance downstream from the grid, the fractal-grid-generated turbulence produced a more turbulent flame with a higher burning rate and a larger flame surface area. Hampp and Lindstedt [30] established that the use of FTG can stabilize the flame in hypersonic conditions, and based on the maximum flame acceleration, they determined the optimal FTG. Hurst and Vassilicos utilized cross-, square-, and I-type FTGs with differing fractal shape parameters to determine length scales [31]. The various length scales result in the formation of a “turbulence development region” where the turbulence or vortex in neighboring areas overlaps until the turbulence intensity decreases after reaching its maximum value. The FTG’s broader turbulence development region causes the peak turbulence intensity to appear further downstream. It is necessary to examine the characteristics of turbulent flow from the turbulence generator to the nozzle exit to comprehend the phenomenon of turbulent flames.

Verbeek et al. [32] analyzed nonreactive turbulent flow and the effect of a change in the shape parameters of cross-and square-type FTGs on a V-shaped turbulent flame. Totaling 24 FTGs, the FTG pattern was varied by altering z (25%, 35%, and 45%), R_t (0.29, 0.4, and 0.7) and N (3 and 4). The shape parameters of the cross-type FTGs were found to affect the trend of the measured turbulence intensity along the central axis, and the turbulence characteristics of the two types of FTGs were evaluated respectively. Additionally, the average turbulence intensity measured along the centerline and off-center was compared to determine

if the turbulence intensity at the central axis could serve as an indicator of the turbulence intensity in regions where a flame is present. The difference between the two values was attributed to the inhomogeneity of the turbulent flow. Maximum relative errors for cross-type and square-type measurements were 16% and 45%, respectively.

While previous research has established the characteristics of fractal grids, little is known about the differences between the effects of fractal geometry's principal parameters with the blockage ratio and the number of fractal pattern iterations on the real scale low-swirl combustor. The objective of this study was to evaluate and compare fractals with different geometries to determine the precise effects of the fractal's figure on the turbulence intensity and other critical parameters of a reacting flow. The CONVERGE package [33] was used, along with a large-eddy simulation $m\sim$ with a dynamic Smagorinsky sub-grid model, and a mesh adaptive technique. Furthermore, CH₄/air premixed combustion was considered in this study, and the SAGE detailed chemical kinetics solver was used to model the combustion.

Chapter 2. Numerical Methods

2.1. Turbulence Model

The governing equations were the unsteady forms for swirling flow applying a spatial and density weighted filter to the conservation equations of mass and momentum, given in Equation 2.1 and 2.2. Because the current study investigated unsteady state flow, the variations of parameters were considered during computational simulation.

Large-eddy simulation (LES) was used for turbulence modeling, and the field was decomposed into a resolved field and a sub-grid field. The resolved field was filtered using spatial average. ρ is the mass density, u is the fluid velocity, P is the pressure, σ is the viscous stress tensor, and τ is sub-grid stress tensor.

$$\frac{\partial \bar{\rho}}{\partial t} + \frac{\partial \bar{\rho} \tilde{u}_i}{\partial x_i} = 0 \quad (2.1)$$

$$\frac{\partial \bar{\rho} \tilde{u}_i}{\partial t} + \frac{\partial \bar{\rho} \tilde{u}_i \tilde{u}_j}{\partial x_j} = -\frac{\partial \bar{P}}{\partial x_i} + \frac{\partial \bar{\sigma}_{ij}}{\partial x_j} - \frac{\partial \tau_{ij}}{\partial x_j} \quad (2.2)$$

The viscous stress tensor σ_{ij} is given by Equation 2.3. μ' is dilatational viscosity, μ is viscosity, and δ_{ij} is Kronecker delta.

$$\sigma_{ij} = \mu \left(\frac{\partial \tilde{u}_i}{\partial x_j} + \frac{\partial \tilde{u}_j}{\partial x_i} \right) + \left(\mu' - \frac{2}{3} \mu \right) \left(\frac{\partial \tilde{u}_k}{\partial x_k} \delta_{ij} \right) \quad (2.3)$$

Furthermore, the mass fraction of all the species was obtained using the species conservation Equation 2.4. D_m is species mass diffusion coefficient, Y_m is mass fraction of species, and S_m is a source term that accounts for combustion.

$$\frac{\partial \bar{\rho}_m}{\partial t} + \frac{\partial \bar{\rho}_m \tilde{u}_j}{\partial x_j} = \frac{\partial}{\partial x_j} \left(\bar{\rho} D_m \frac{\partial Y_m}{\partial x_j} \right) + S_m \quad (2.4)$$

The sub-grid stress tensor τ_{ij} is given by Equation 2.5.

$$\tau_{ij} = \bar{\rho} (\tilde{u}_i \tilde{u}_j - \tilde{u}_i \tilde{u}_j) \quad (2.5)$$

The dynamic Smagorinsky model is a zero-equation LES model that can be used for determining the local value of the Smagorinsky coefficient [34-36]. For calculating the Smagorinsky constant, the grid filter, Δ and the test filter, $\hat{\Delta}$ which is typically twice the value of the grid filter were used. T_{ij} is double filtering residual stress, and L_{ij} is Leonard stress term.

$$L_{ij} = T_{ij} - \widehat{\tau}_{ij} \quad (2.6)$$

The Smagorinsky model of the deviatoric part of L_{ij} can be expressed as Equation 2.7. $C_{s-dynamic}$ is the dynamic Smagorinsky coefficient.

$$L_{ij} - \frac{1}{3}L_{kk}\delta_{ij} = C_{s-dynamic}M_{ij} \quad (2.7)$$

The sub-grid scale stress tensor changed from Equation 2.5 to 2.8. and S_{ij} is the rate of strain tensor.

$$\tau_{ij} = -2C_{s-dynamic}\bar{\Delta}^2 \left| \widehat{S} \right| \widehat{S}_{ij} \quad (2.8)$$

The dynamic Smagorinsky model determines model constant dynamically. The finite volume method was used to solve the momentum equation, and pressure-velocity coupling was achieved using the modified pressure implicit with splitting of operator (PISO) method of Issa [37].

2.2. Combustion Model

The SAGE detailed chemical kinetics solver uses the CVODE solver, which is part of the Suite of Nonlinear and Differential/Algebraic Equation Solvers (SUNDIALS) package, to solve systems of ordinary differential equations (ODEs). It solves detailed chemical kinetics by using a set of CHEMKIN-formatted input files. While transport equations are solved, SAGE calculates the reaction rates for each elementary reaction. As described by Turns [38], a multistep chemical reaction mechanism can be written in the form

$$\sum_{m=1}^M v'_{m,i} \chi_m \rightleftharpoons \sum_{m=1}^M v''_{m,i} \chi_m \text{ for } i = 1, 2, \dots, I \quad (2.9)$$

v' is stoichiometric coefficients of the reactants, v'' is stoichiometric coefficients of the products, and χ_m is chemical symbol for species m . The net production rate of species m is given by

$$\dot{\omega}_m = \sum_{i=1}^I (v''_{m,i} - v'_{m,i}) q_i \text{ for } m = 1, 2, \dots, M \quad (2.10)$$

The rate-of-progress parameter q_i for the i -th reaction is

$$q_i = k_{i,f} \prod_{m=1}^M [X_m]^{v'_{m,i}} - k_{i,r} \prod_{m=1}^M [X_m]^{v''_{m,i}} \quad (2.11)$$

$[X_m]$ is the molar concentration of species m , and $k_{i,f}$ and $k_{i,r}$ are the forward and reverse rate coefficients for reaction i . The forward rate coefficient is expressed in Arrhenius form as

$$k_{i,f} = A_i T^{\beta_i} \exp\left(-\frac{E_i}{RT}\right) \quad (2.12)$$

A_i is the pre-exponential factor, β_i is the temperature exponent, E_i is the activation energy (in *cal/mol*), T is the temperature and R is the ideal gas constant.

2.3. Computational Domain

The low-swirl combustor configuration used in this study is shown in Fig. 2.1, and it was based on a real scale combustor geometry. The fully premixed reactant flow entered the inlet and was divided into two parts, namely a core section (plate) and an annular section (swirl). These two flows were combined after the burner, and the combined flow exited the nozzle through the recess section. Specifically, the burner was composed of the turbulence generating plate (outer diameter: 79.9 mm, inner diameter: 73.9 mm) which was positioned in front of the swirler and the swirler (16 vanes, vane angle $\alpha = 40^\circ$). The actual chamber length of the low-swirl combustor surpassed 1000 mm, but due to the limited number of grids, we adjusted the chamber length to three times the chamber diameter.

We designated each section of the burner and chamber with five names (Z1–Z5) to provide a clearer explanation, as shown in the square in Fig. 2.2. Z1 is right after the turbulence generating plate, and Z2 becomes the entrance of swirler. Furthermore, Z3 and Z4 indicate the steps in which the outer recirculation zones were formed in front of dump plate. At last, Z5 represents the reaction zone of the chamber.

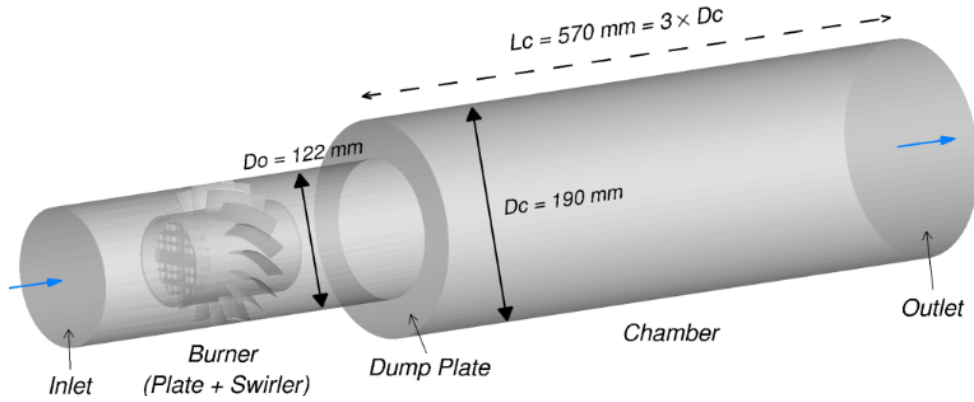


Figure 2.1 Computational domain of the real scale low-swirl combustor

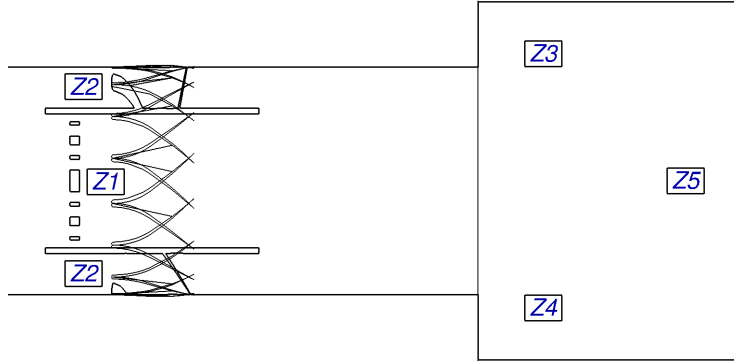


Figure 2.2 Name $Z1 - Z5$ to burner and chamber section

Figure 2.3 and 2.4 describes the dimensions of the fractal cross pattern. Also, Table 1 and Figure 2.5 shows the four types of plate specifications and geometries used in this study. Each fractal cross plate was perfectly defined by four parameters: t_0 (the thickness of the central cross bar), L_0 (the inner diameter of the plate), N (the number of iterations), and R_t ($= t_{i+1}/t_i$; the ratio between continuous bar thicknesses) [20]. The thickness of the central cross bar, t_0 , among plates can be different because we focused on the different iteration number for a given blockage ratio.

The CH₄/Air premixed mixture equivalence ratio was 0.49, and the temperature was 723 K. We set the mass flow rate 0.446 kg/s instead of setting the inlet velocity. The inlet pressure had zero normal gradient, and the outlet pressure was set to be 1.48 bar. Furthermore, the combustion chamber wall temperature was 1000 K, and the dump plate's temperature was 723 K, identical to the inlet's temperature. The no-slip condition was imposed on all walls.

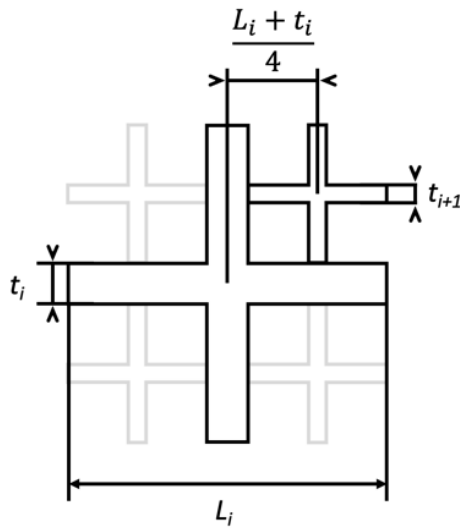
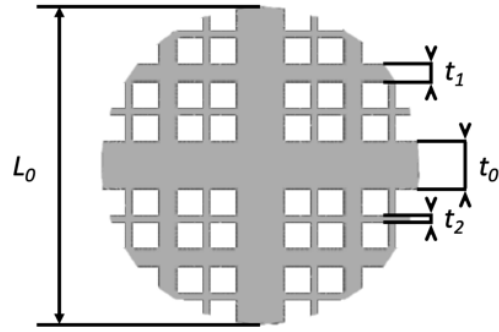


Figure 2.3 Definition of the fractal cross pattern [21]

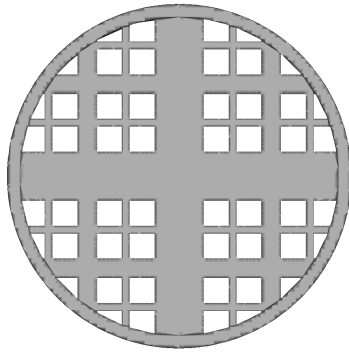


六

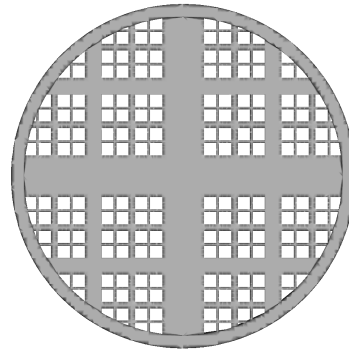
Figure 2.4 Definition of circular cropped fractal grid with three iterations [21]

Table 2.1 Characteristics of turbulence generating plate

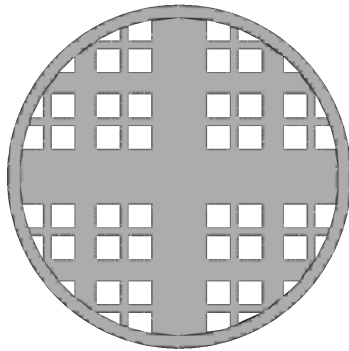
	Case 1	Case 2	Case 3	Case 4
σ	67%	67%	73%	73%
t_0 [mm]	11.4	9.7	12.9	11.0
N	3	4	3	4
R_t	0.4	0.4	0.4	0.4



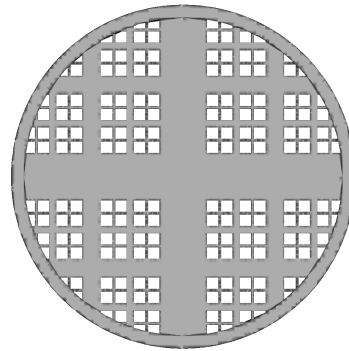
Case 1



Case 2



Case 3



Case 4

Figure 2.5 Four types of turbulence generating plate

2.4. Adaptive Mesh Refinement

Adaptive mesh refinement (AMR) refines the grid size automatically based on fluctuating and moving conditions such as temperature or velocity. It obtains a refined grid in flow regions of interest allowing complex phenomenon, such as flame propagation or high-velocity flow.

The basic mesh size was set to 4mm, and the minimum size of the grid is 1mm in three dimensions computational domain. Near the burner and the combustion area in chamber, where the importance of flow increased, embedded mesh refinement was performed. The number of maximum grids is 10 million. Based on the sub-grid field AMR theory, velocity criterion is 1 m/s and temperature criterion is 2.0 K.

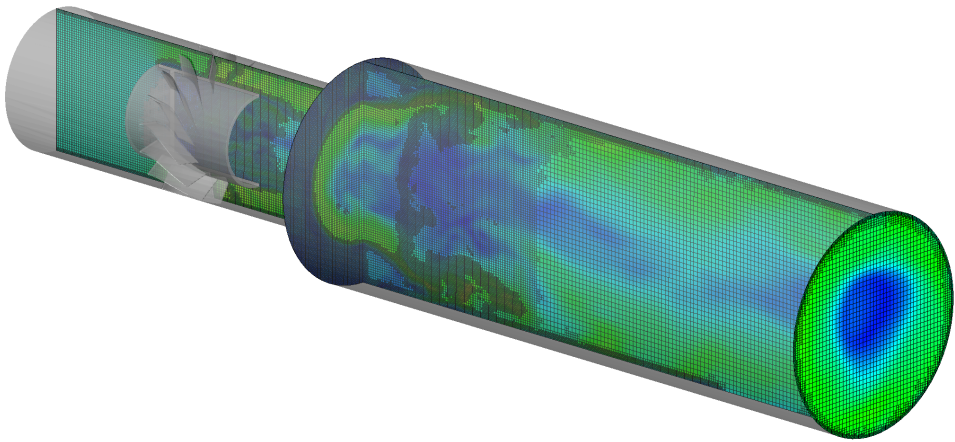


Figure 2.6 Velocity field with adaptive mesh refinement

Chapter 3. Validation Study

3.1. Swirl Number

The swirl number is a nondimensional number of the swirl flow's intensity. It defines the ratio of the angular momentum to linear momentum and illustrates it with Equation 3.1. This theoretical definition of the swirl number cannot be used in an experimental flow momentum. The equation of the swirl number can be rewritten as Equation 3.2 with the burner geometry and the assumptions which were the distribution of the axial flow remained flat and $\tan\alpha$ was identical to U/W at the burner exit, where α is the blade angle.

$$SN = \frac{\int_{R_c}^{R_b} \rho U W r^2 dr}{R_b (\int_{R_c}^{R_b} \rho U^2 dr + \int_0^{R_c} \rho U_c^2 r dr)} \quad (3.1)$$

$$N = \frac{2}{3} \tan\alpha \frac{1 - R^3}{1 - R^2 + \left[m^2 \left(\frac{1}{R^2} - 1 \right)^2 \right] R^2} \quad (3.2)$$

R is the ratio of the centerbody radius to the burner radius ($R = R_c/R_b$) and the mass flux ratio m is the ratio of the centerbody's mass

flux to the annular mass flux ($m = \dot{m}_c/\dot{m}_a$). In Equation 3.2, we calculate the mass flux ratio m using mass integration, and the area ratio can be easily acquired from the configuration; mass integration was performed using the computational simulation results obtained in the present study. Figure 3.1 shows a comparison between the present numerical results and the experimental data. Evidently, the numerical results could predict the swirl number with high accuracy for all cases.

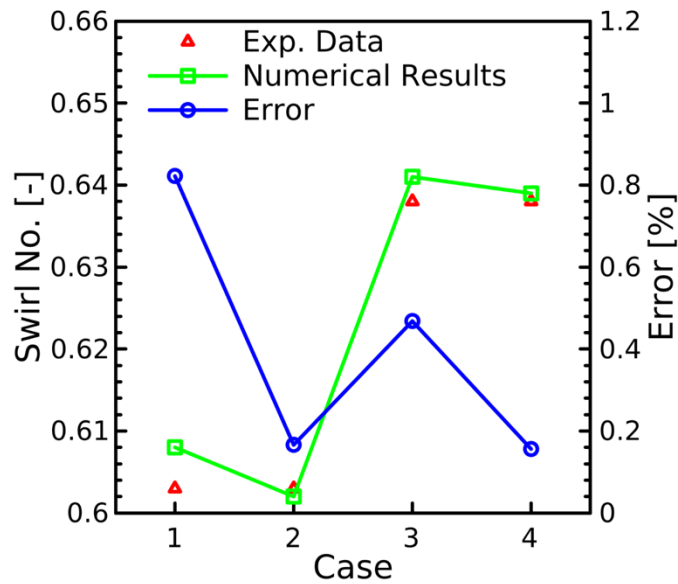


Figure 3.1 Swirl number comparison between numerical results and experimental data

Chapter 4. Results and Discussion

4.1. Nonreacting Mode

4.1.1. Velocity Field

This section analyzes the effects of fractal geometry on nonreacting flow. The objective of the analysis is to determine the best fractal geometry in terms of turbulence intensity, which is one of the major factors that determine the combustion performance. In general, the existence of fractal plate changes the flow streamline as evident in Fig. 4.1, because few streamlines obstructed by the fractal plate deviate from the central axial direction.

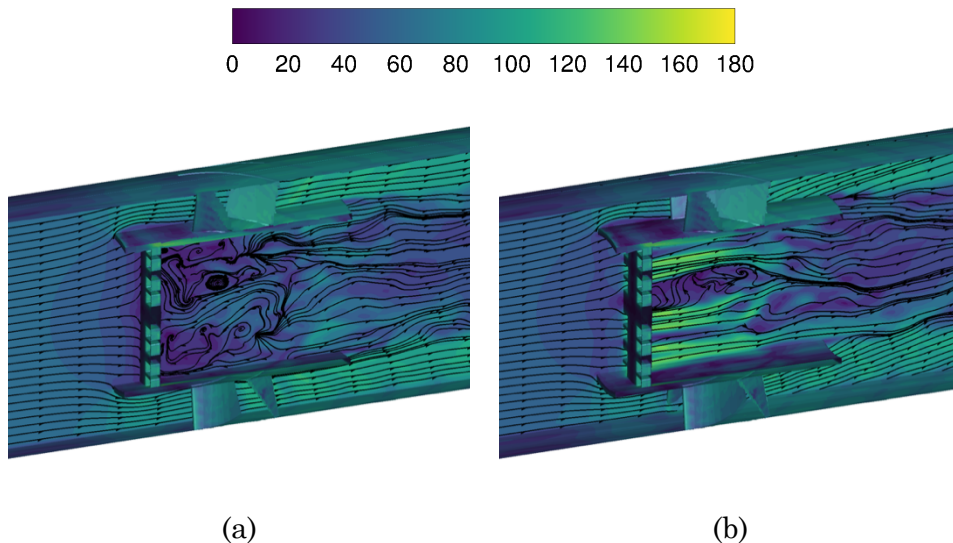
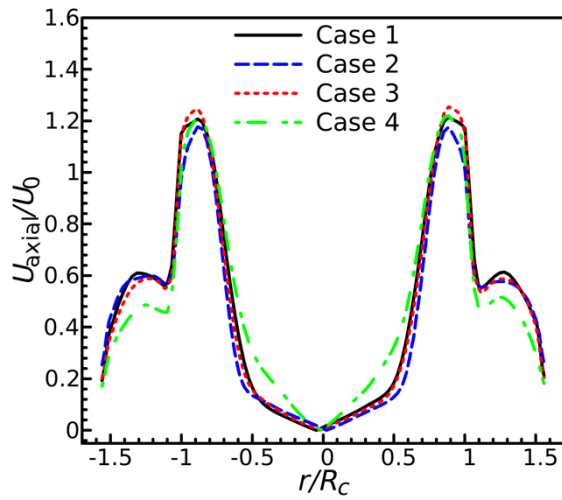
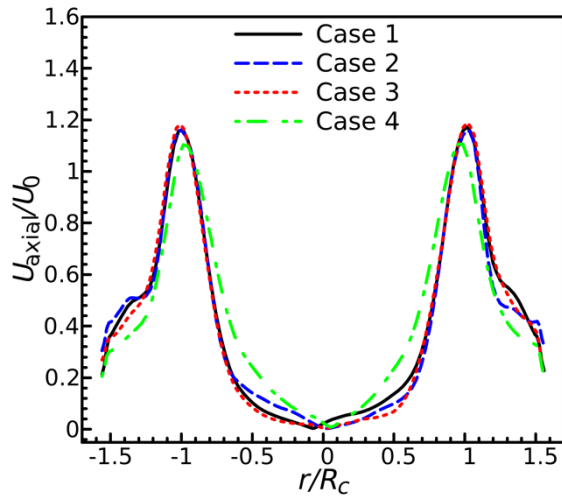


Figure 4.1 The cross section of flow direction deviation through the blocked part of plate (a) and the hole part of plate (b) in Case 1

This deviation is determined by the size of the fractal plate's holes. Figure 4.2 depicts the axial velocity distribution in a direction perpendicular to the flow at dimensionless axial distances 0.1, 0.2, 0.3, and 0.4 from the burner exit. Apparently, the Case 4 indicates that $Z5$ has the greatest axial velocity, whereas $Z3$ and $Z4$ have the lowest velocity. Owing to the small area of the hole at fractal plate and the law of conservation of mass, the decrease in area led to an increase the local velocity in the region following the fractal plate ($Z1$), while the velocity is significantly reduced in the front of the burner's annular section ($Z2$), as depicted in Fig. 4.3. Because of the incompressibility of the flow, Fig. 4.1 shows that any change to the fractal plate brings an immediate influence on velocity variation, and Case 4 shows the largest difference between the maximum and minimum velocities. Furthermore, Fig. 4.2 reveals that Case 4 differs significantly more than the other cases, notably at $Z/d = 0.1$, indicating that the velocity gradient dominates in Case 4. Since the combustion begins in the $Z3$ and $Z4$ regions of the reacting flow, decreasing the velocity in these regions enhances the turbulence intensity. This explains the inverse relationship between the velocity and the turbulence intensity. Reducing the velocity also increases the residence time of the flow; consequently, the mixing time for combustion flow increases, resulting in more complete combustion.

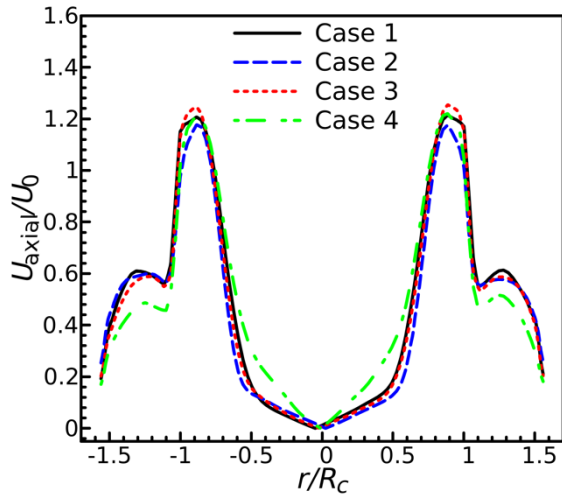


(a) $Z/d = 0.1$

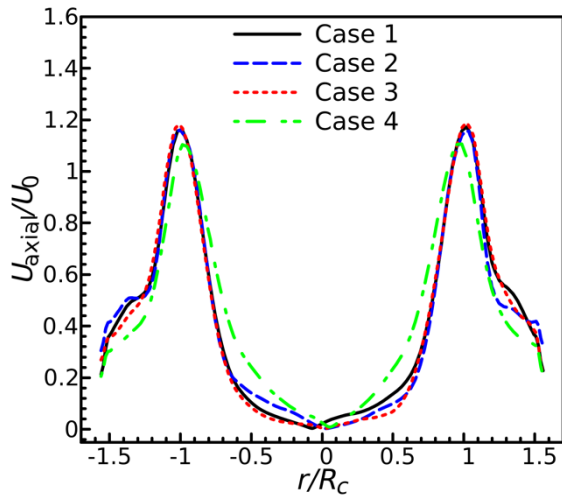


(b) $Z/d = 0.2$

Figure 4.2 Axial velocity distribution at various axial distances perpendicular to the flow



(c) $Z/d = 0.3$



(d) $Z/d = 0.4$

Figure 4.2 Axial velocity distribution at various axial distances perpendicular to the flow

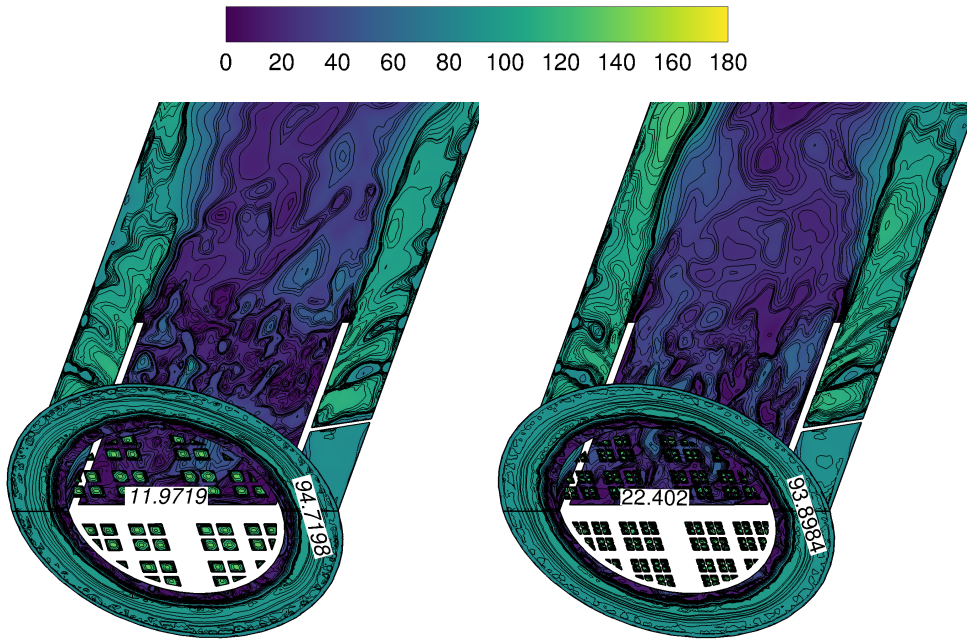


Figure 4.3 Flow velocity distribution in Case 3 and Case 4

This page intentionally left blank

4.1.2. Vorticity Field

The contours in Fig. 4.4 depict the vorticity distribution in each of the four cases. We mentioned that Case 4 had a larger velocity gradient than the other cases, which is evident in Fig. 4.2. By increasing the velocity gradient and the velocity differences on both sides of the shear layer, the vorticity in Case 4 is significantly larger than those in the other cases. This peculiarity renders the flow unstable and modifies the flame's behavior in the reacting mode. The vorticity and flow instability are two of the most crucial factors that accelerate the mixing of the reacting flow and increase the combustion efficiency.

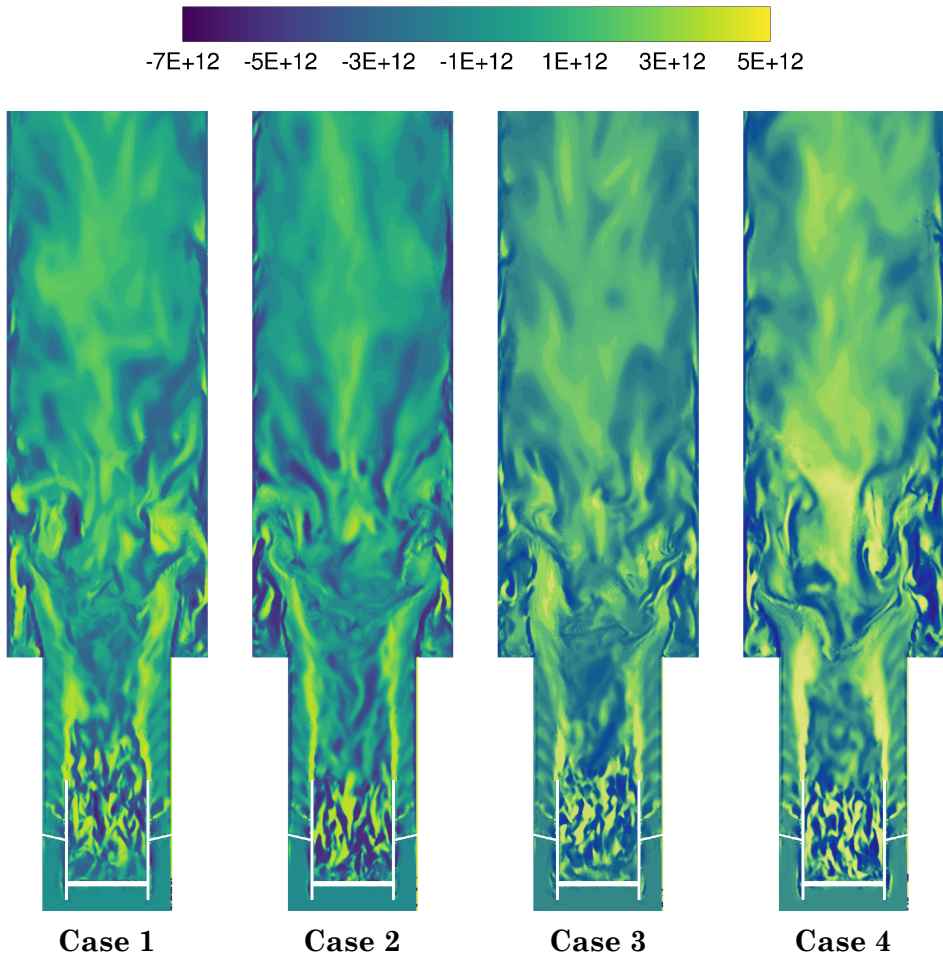
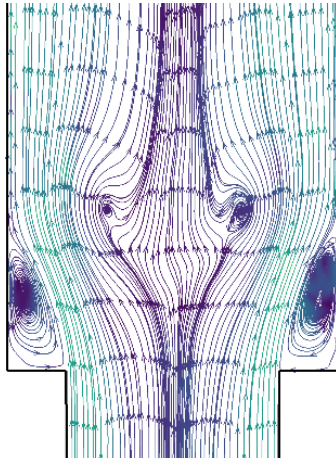


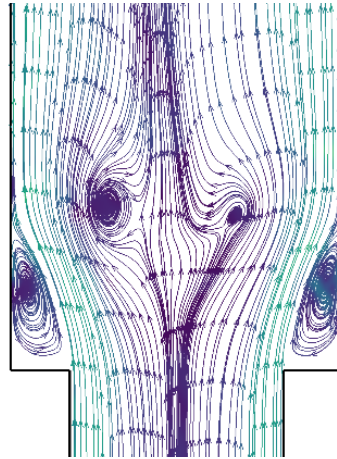
Figure 4.4 Instantaneous vorticity distribution for all cases

4.1.3. Streamline

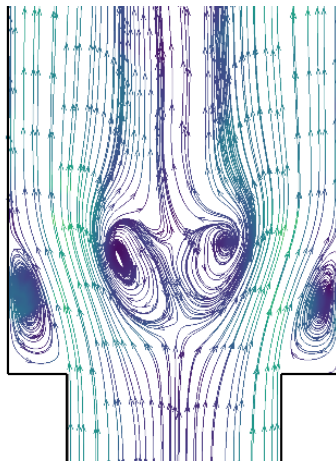
Figure 4.5 depicts the streamline of the average velocity flow fields. All streamlines exhibit similar diverging flow structure because the swirl intensities are deliberately low. Such similarity cannot be seen during the strong recirculation-related vortex breakdown process. The IRZ at the center and the ORZ in front of the dump plate are separated by two shear layers. In the inner and outer shear layers, there are significant velocity gradients. The size of the IRZ in Case 1 and 2 (67% blockage ratio) was smaller than those in Case 3 and 4 (73% blockage ratio), resulting in a top-flow-width disparity. There were interactions between IRZs not in 67% blockage ratio group but in 73% blockage ratio group. Because the central flow in 67% blockage ratio group passed through the midpoint, and the stagnation point identified in front of IRZs. In 73% blockage ratio group, as the IRZs were grown up, the stagnation point is formed closer to nozzle exit IRZs. In 67% blockage ratio group, the location of IRZ center is farther from the nozzle exit compared with 73% blockage ratio group. The ORZs did not distinguish among any of all cases. These characteristics can be explained together with the results of swirl number. In general, the inner recirculation zone only occurs when the swirl number is bigger than 0.6 ($S > 0.6$). As the given blockage ratio, the swirl number is slightly bigger than 0.6. It means that the characteristics of low-swirl combustion begin to disappear in all cases. These phenomena promote flame stability and flame lift-off during reacting flow.



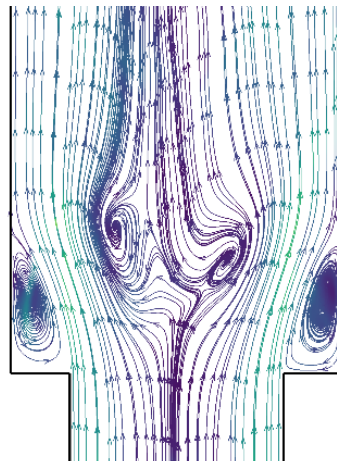
Case 1



Case 2



Case 3



Case 4

Figure 4.5 Streamline of average velocity flow fields for all cases

4.2. Reacting Mode

4.2.1. Hydroxide (OH) mole fraction

In the nonreacting section, it was shown that Case 4 and 3 were the best and worst cases, respectively, from the standpoint of generating the turbulence intensity. This section discusses an investigation of the combustion flow behavior for these two cases.

Figure 5.1 depicts the distribution of the mole fraction of free OH radical, which was an intermediate species. The OH mole fraction distribution indicates the reaction's location and the amount of heat released. During the combustion process, the extracted H atom combined with an O atom to form the OH radical through elementary reactions such as $\text{CH}_2\text{O} + \text{OH} \leftrightarrow \text{CHO} + \text{H}_2\text{O}$ and $\text{CO} + \text{OH} \leftrightarrow \text{CO}_2 + \text{H}$. It is evident that Case 4 has a significantly larger area containing that maximum value of OH radical than Case 3, indicating that Case 4 should be used to achieve more complete combustion and reduce the amount of unburned fuel at the chamber exit.

Consequently, an increase in the amount of OH radical indicates that the area of the weakened reaction zone has been considerably reduced by using Case 4, since the fractal structure of Case 4 reduces the reaction zone's velocity as described in the previous section. The principal factor responsible for reducing the weakened reaction zone is the reduction in shear strain.

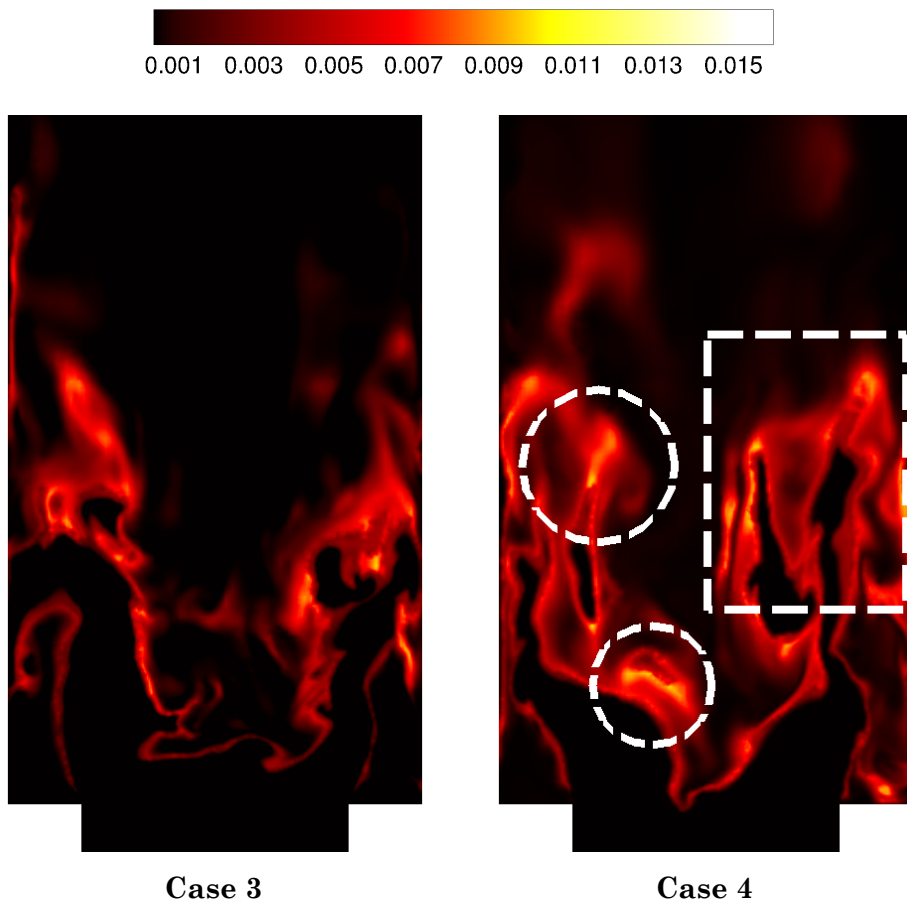


Figure 5.1 Hydroxide (OH) mole fraction distribution in Case 3 and Case 4

Furthermore, it was found that Case 4 increased the flow residence time, providing the combustion mixture more time to react. The distribution of OH showed that the energy release occurred closer to the reaction zone in Case 4, implying that this case makes the reaction zone better.

4.2.2. Formaldehyde (CH₂O) mole fraction

Another important intermediate species is formaldehyde (CH₂O), which is typically present in preheated zones. This species is produced by the decomposition of hydrogen atoms during the combustion of CH₄ [39]. Its presence indicates an accelerated rate of fuel decomposition as well as an increase in the amount of heat released [40]. Figure 5.2 shows that for Case 4, the CH₂O mole fraction became more uniform and CH₂O gradients disappeared. This behavior reconfirms that the reaction zone expanded significantly and had a larger volume in Case 4. It should be noted that CH₂O and OH can be related by such as $\text{CH}_3 + \text{O}_2 \leftrightarrow \text{OH} + \text{CH}_2\text{O}$, $\text{O} + \text{CH}_2\text{O} \leftrightarrow \text{OH} + \text{HCO}$, and $\text{O} + \text{CH}_3\text{O} \leftrightarrow \text{OH} + \text{CH}_2\text{O}$. When Case 4 is used, the highest CH₂O mole fraction region is clearly reduced, and because low amounts of CH₂O are found in zones with high temperatures, the reaction rates in these zones are increased. Therefore, the fuel decomposition of the combustible mixture in Case 4 is faster than that in Case 3. Furthermore, according to the CH₂O distribution, the maximum value of CH₂O formation is greater for Case 4 compared with that for Case 3, indicating an increase in preheating and energy release.

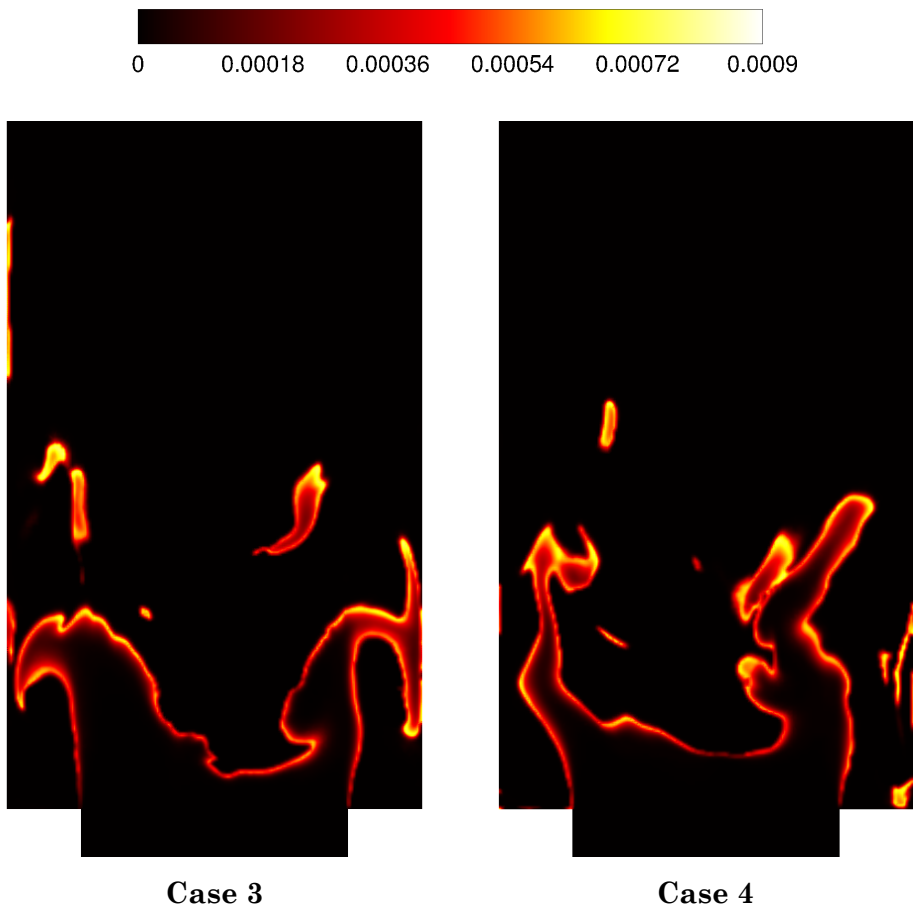


Figure 5.2 Formaldehyde (CH_2O) mole fraction distribution in Case 3 and Case 4

4.2.3. Hydroperoxyl (HO₂) mole fraction

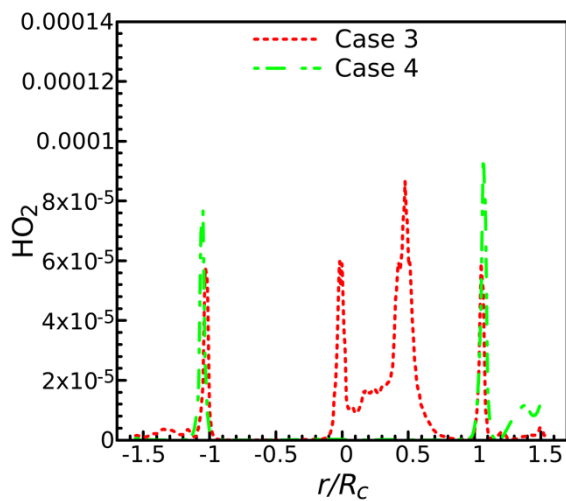
The radial variation of the hydroperoxyl (HO₂) radical in Case 3 and 4 is depicted in Fig. 5.3. This radical represents the recombination process in the reacting flow [41,42], and it is a key species in the ignition process [43]. Its formation depends on the production of CH₂O, O₂, H₂O, N₂, OH, and HCO, as shown in Table 2.

Case 4 increases the amount of OH and CH₃OH as discussed earlier in this paper. Case 3 has a greater concentration of HO₂ species than Case 4 at distances close to the inlet zone (*Z5*) and along the centerline of the burner, as shown in Fig. 11. Case 4 has a slightly higher concentration of HO₂ radical in the *Z3* and *Z4* (recirculation zones) regions of the burner.

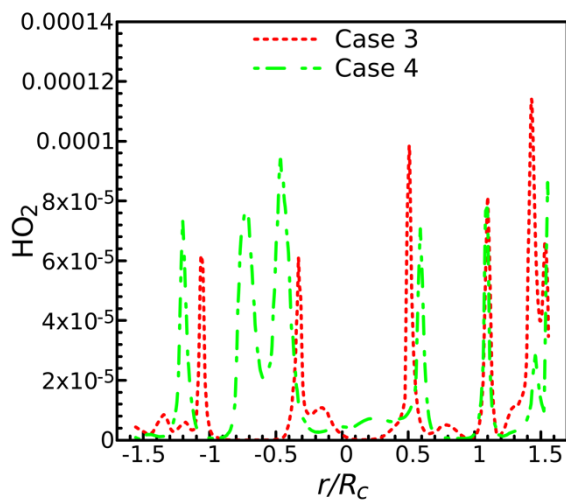
Furthermore, an analysis of variations in the HO₂ radical at various vertical locations showed that the amount of HO₂ in Case 3 was more than that in Case 4 and that it had a direct effect on the NO emissions of the burner. HO₂ has been shown to be strongly correlated with the rapid production of NO during hydrocarbon fuel combustion [44,45]. Figure 5.4 depicts the average NO emission mass fraction at the burner outlet zone for Case 3 and 4. Case 4 clearly reduces NO emissions and prompt NO apparently plays a significant role in the reduction of average NO emissions.

Table 2. Reaction mechanisms that produce HO₂ species [44]

1	2	3	4	5	6	7	8
$O_2 + CH_2O \rightleftharpoons HO_2 + HCO$	$2H + O_2 + M \rightleftharpoons HO_2 + M$	$OH + HO_2 \rightleftharpoons O_2 + H_2O$	$H_2 + O_2 \rightleftharpoons HO_2 + O_2$	$H + O_2 + H_2O \rightleftharpoons HO_2 + H_2O$	$H + O_2 + N_2 \rightleftharpoons HO_2 + N_2$	$OH + H_2O_2 \rightleftharpoons HO_2 + H_2O$	$HCO + O_2 \rightleftharpoons HO_2 + CO$

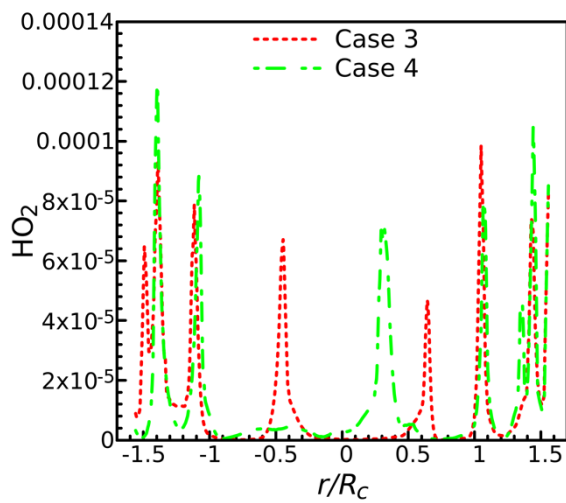


(a) $Z/d = 0.1$

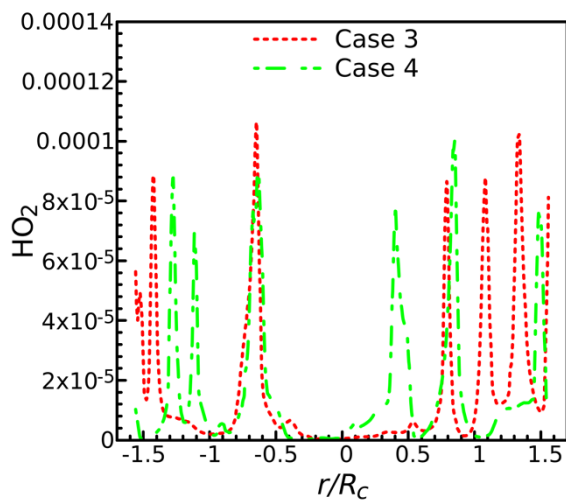


(b) $Z/d = 0.2$

Figure 5.3 Radial variation of the Hydroperoxyl (HO_2) radical in Case 3 and Case 4



(c) $Z/d = 0.3$



(d) $Z/d = 0.4$

Figure 5.3 Radial variation of the Hydroperoxyl (HO_2) radical in Case 3 and Case 4.

4.2.4. Emission Gas

As stated, improved mixing, increased reactive mixture residence time, and increased turbulence intensity all contribute to more complete combustion. Consequently, it is expected that the amount of NO emissions will decrease if Case 4 is implemented, unlike Case 3. A reduction in pollutants such as NO and CO is one of the most advantageous effects of an efficient combustion process. Figure 5.4 depicts the quantity of NO emission gas reduction at the outlet but CO. Using Case 4 to increase the turbulence intensity and vorticity results in an increase in the reactivity of the reacting flow, and it can be stated that the combustive flow is exposed to a higher power and helps decompose the emission species once more.

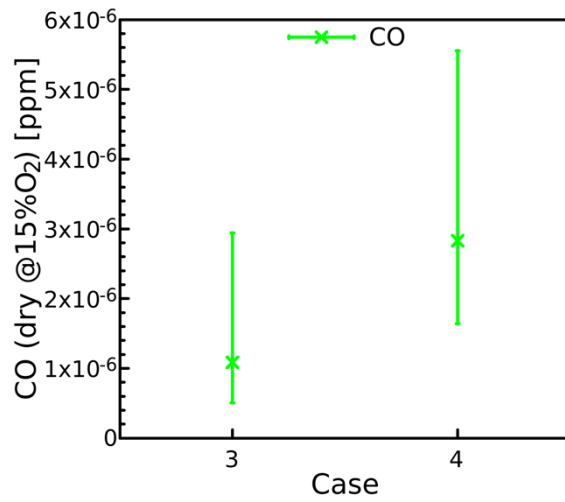
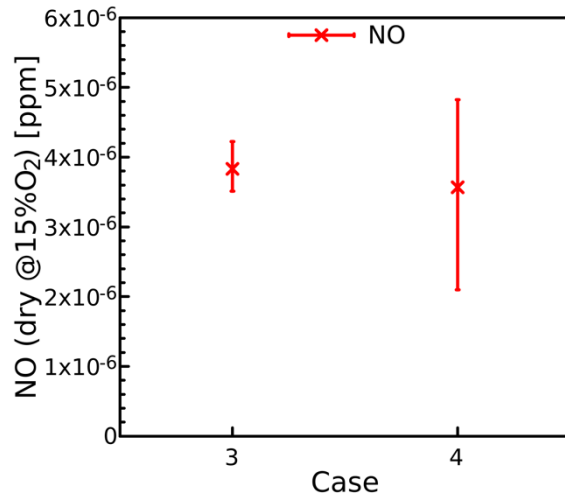


Figure 5.4 NO and CO emissions in Case 3 and Case 4

Chapter 5. Conclusion

A large-eddy simulation was performed using CONVERGE for a real scale low-swirl combustor. The numerical results show high agreement with experimental data about swirl number. Fractal-patterned was adopted to use turbulence generating plate. In addition, the effects of fractal geometry on the main flow for the nonreacting and reacting mode were investigated. The acquired results are summarized below.

- Case 4 had the highest axial velocity in the inner recirculation zone and the lowest axial velocity at the location of the shear layer.
- Case 4 showed the largest difference between the maximum and minimum local velocity values. This implies that the velocity gradient increased when Case 4 was used. Case 4 decreased the velocity at the location of the starting point of combustion, and the inverse relation between velocity and turbulence intensity indicates that it enhances the turbulence intensity. Furthermore, reducing the velocity increased the residence time of the flow; consequently, the mixing time for the combustion flow increased, resulting in more complete combustion.

- The vorticity in Case 4 was significantly higher than in the other cases. This peculiarity rendered the flow unstable and speeded up the mixing of the reacting flow, which enhanced the combustion efficiency.
- The fractal plate with a 67% blockage ratio had a smaller inner recirculation zone than the fractal plate with a 73% blockage ratio, which resulted in a top-flow width disparity. Additionally, the inner recirculation zone was closer to the nozzle exit when a 73% blockage ratio was used. These phenomena result in high flame stability and flame lift-off during reacting flow.
- Case 4 showed a remarkably larger area with the maximum value of OH compared with Case 3. This observation indicated that Case 4 could be used to achieve more complete combustion and to reduce the amount of unburned fuel at the chamber exit.
- Using Case 4 reduced the size of the weakened reaction zone (compared with Case 3) since the fractal structure of Case 4 caused the reaction zone's velocity (shear strain) to decrease.

- The use of Case 4 caused the CH₂O mole fraction to become more uniform and the disappearance of CH₂O gradients. These observations indicated that when Case 4 is used, the reaction zone expands significantly and therefore has a larger volume. Furthermore, based on the CH₂O distribution, the maximum value of CH₂O formation was found to be greater in Case 4 compared with Case 3, indicating an increase in preheating and energy release. Thus, using Case 4 reduces NO emissions.

Bibliography

- [1] Cheng, R. K. "Low swirl combustion," *The Gas Turbine Handbook*, 2006, pp. 241-255.

- [2] Cafiero, G., Discetti, S., and Astarita, T. "Heat transfer enhancement of impinging jets with fractal-generated turbulence," *International Journal of Heat and Mass Transfer* Vol. 75, 2014, pp. 173-183.

- [3] Cafiero, G., Greco, C. S., Astarita, T., and Discetti, S. "Flow field features of fractal impinging jets at short nozzle to plate distances," *Experimental Thermal and Fluid Science* Vol. 78, 2016, pp. 334-344.

- [4] Jiang, S., Wang, J., Feng, L.-F., and Coppens, M.-O. "Fractal injectors to intensify liquid-phase processes by controlling the turbulent flow field," *Chemical Engineering Science* Vol. 238, 2021, p. 116616.

- [5] Zheng, S., Bruce, P. J. K., Cuvier, C., Foucaut, J. M., Graham, J. M. R., and Vassilicos, J. C. "Nonequilibrium dissipation scaling in large Reynolds number turbulence generated by rectangular fractal grids," *Physical Review Fluids* Vol. 6, No. 5, 2021, p. 054613.

- [6] Simmons, L. F. G., Salter, C., and Taylor, G. I. "Experimental investigation and analysis of the velocity variations in turbulent flow," *Proceedings of the Royal Society of London. Series A, Containing Papers of a Mathematical and Physical Character* Vol. 145, No. 854, 1934, pp. 212-234.
- [7] Gad-El-Hak, M., and Corrsin, S. "Measurements of the nearly isotropic turbulence behind a uniform jet grid," *Journal of Fluid Mechanics* Vol. 62, No. 1, 1974, pp. 115-143.
- [8] Seoud, R. E., and Vassilicos, J. C. "Dissipation and decay of fractal-generated turbulence," *Physics of Fluids* Vol. 19, No. 10, 2007, p. 105108.
- [9] Isaza, J. C., Salazar, R., and Warhaft, Z. "On grid-generated turbulence in the near-and far field regions," *Journal of Fluid Mechanics* Vol. 753, 2014, pp. 402-426.
- [10] Valente, P., and Vassilicos, J. "The non-equilibrium region of grid-generated decaying turbulence," *Journal of Fluid Mechanics* Vol. 744, 2014, pp. 5-37.
- [11] Yang, Y., Ting, D. S.-K., and Ray, S. "Improving Heat Transfer Efficiency with Innovative Turbulence Generators," *Climate Change and Pragmatic Engineering Mitigation*. Jenny Stanford Publishing, 2022, pp. 131-160.

- [12] Cafiero, G., Castrillo, G., Greco, C. S., and Astarita, T. "Effect of the grid geometry on the convective heat transfer of impinging jets," *International Journal of Heat and Mass Transfer* Vol. 104, 2017, pp. 39-50.
- [13] Hoi, S. M., Ooi, E. H., Chew, I. M. L., and Foo, J. J. "SPTV sheds light on flow dynamics of fractal-induced turbulence over a plate-fin array forced convection," *Scientific Reports* Vol. 12, No. 1, 2022, pp. 1-20.
- [14] Goh, K. H. H., Geipel, P., and Lindstedt, R. P. "Lean premixed opposed jet flames in fractal grid generated multiscale turbulence," *Combustion and Flame* Vol. 161, No. 9, 2014, pp. 2419-2434.
- [15] Es-Sahli, O., Sescu, A., Afsar, M. Z., and Buxton, O. R. H. "Investigation of wakes generated by fractal plates in the compressible flow regime using large-eddy simulations," *Physics of Fluids* Vol. 32, No. 10, 2020, p. 105106.
- [16] Cafiero, G., Discetti, S., and Astarita, T. "Flow field topology of submerged jets with fractal generated turbulence," *Physics of Fluids* Vol. 27, No. 11, 2015, p. 115103.
- [17] Nedic, J., Ganapathisubramani, B., Vassilicos, J. C., Borée, J., Brizzi, L. E., and Spohn, A. "Aeroacoustic Performance of Fractal Spoilers," *AIAA Journal* Vol. 50, No. 12, 2012, pp. 2695-2710.

- [18] Laizet, S., and Vassilicos, J. C. "Stirring and scalar transfer by grid-generated turbulence in the presence of a mean scalar gradient," *Journal of Fluid Mechanics* Vol. 764, 2015, pp. 52-75.
- [19] Kim, J., Kim, J., and Han, C. Y. "Experimental Study of Turbulent Flow in a Circular Jet with Different Types of Fractal Turbulence Generators," *Available at SSRN 4091195*, 2022.
- [20] Giannadakis, A., Naxakis, A., Romeos, A., Perrakis, K., and Panidis, T. "An experimental study on a coaxial flow with inner swirl: Vortex evolution and flow field mixing attributes," *Aerospace Science and Technology* Vol. 94, 2019, p. 105373.
- [21] Verbeek, A. A., Bouten, T. W. F. M., Stoffels, G. G. M., Geurts, B. J., and van der Meer, T. H. "Fractal turbulence enhancing low-swirl combustion," *Combustion and Flame* Vol. 162, No. 1, 2015, pp. 129-143.
- [22] Van der Lans, R. P., Glarborg, P., and Dam-Johansen, K. "Influence of process parameters on nitrogen oxide formation in pulverized coal burners," *Progress in Energy and Combustion Science* Vol. 23, No. 4, 1997, pp. 349-377.
- [23] Wu, J., Zhang, M.-c., Fan, H.-J., Fan, W.-d., and Zhou, Y.-g. "A study on fractal characteristics of aerodynamic field in low-NO_x coaxial swirling burner," *Chemical Engineering Science* Vol. 59, No. 7, 2004, pp. 1473-1479.

- [24] Kabiraj, L., Saurabh, A., Karimi, N., Sailor, A., Mastorakos, E., Dowling, A. P., and Paschereit, C. O. "Chaos in an imperfectly premixed model combustor," *Chaos: An Interdisciplinary Journal of Nonlinear Science* Vol. 25, No. 2, 2015, p. 023101.
- [25] Balakrishnan, P., and Srinivasan, K. "Influence of swirl number on jet noise reduction using flat vane swirlers," *Aerospace Science and Technology* Vol. 73, 2018, pp. 256-268.
- [26] Cheng, W., Wang, Z., Zhou, L., Shi, J., and Sun, X. "Infrared signature of serpentine nozzle with engine swirl," *Aerospace Science and Technology* Vol. 86, 2019, pp. 794-804.
- [27] Zhou, L., and Luo, K. "Studies on a swirling heptane spray flame by large-eddy simulation," *Aerospace Science and Technology* Vol. 126, 2022, p. 107632.
- [28] Zhou, L. X. "Comparison of studies on flow and flame structures in different swirl combustors," *Aerospace Science and Technology* Vol. 80, 2018, pp. 29-37.
- [29] Soulopoulos, N., Kerl, J., Sponfeldner, T., Beyrau, F., Hardalupas, Y., Taylor, A. M. K. P., and Vassilicos, J. C. "Turbulent premixed flames on fractal-grid-generated turbulence," *Fluid Dynamics Research* Vol. 45, No. 6, 2013, p. 061404.

- [30] Hampp, F., and Lindstedt, R. P. "Fractal Grid Generated Turbulence—A Bridge to Practical Combustion Applications," *Fractal Flow Design: How to Design Bespoke Turbulence and Why*. Springer International Publishing, Cham, 2016, pp. 75-102.
- [31] Hurst, D., and Vassilicos, J. C. "Scalings and decay of fractal-generated turbulence," *Physics of Fluids* Vol. 19, No. 3, 2007, p. 035103.
- [32] Verbeek, A. A., Willems, P. A., Stoffels, G. G. M., Geurts, B. J., and van der Meer, T. H. "Enhancement of turbulent flame speed of V-shaped flames in fractal-grid-generated turbulence," *Combustion and Flame* Vol. 167, 2016, pp. 97-112.
- [33] Richards, K., Senecal, P., and Pomraning, E. "CONVERGE documentation (Version 3.0)," *Madison, WI: Convergent Science*, 2016.
- [34] Lilly, D. K. "A proposed modification of the Germano subgrid-scale closure method," *Physics of Fluids A: Fluid Dynamics* Vol. 4, No. 3, 1992, pp. 633-635.
- [35] Germano, M., Piomelli, U., Moin, P., and Cabot, W. H. "A dynamic subgrid-scale eddy viscosity model," *Physics of Fluids A: Fluid Dynamics* Vol. 3, No. 7, 1991, pp. 1760-1765.
- [36] Meneveau, C. "Statistics of turbulence subgrid-scale stresses: Necessary conditions and experimental tests," *Physics of Fluids* Vol. 6, No. 2, 1994, pp. 815-833.

- [37] Issa, R. I. "Solution of the implicitly discretised fluid flow equations by operator-splitting," *Journal of Computational Physics* Vol. 62, No. 1, 1986, pp. 40-65.
- [38] Turns, S. R. *An Introduction to Combustion: Concepts and Applications*. London: McGraw-Hill Education - Europe, 2011.
- [39] Mousavi, S. M., Sotoudeh, F., Jun, D., Lee, B. J., Esfahani, J. A., and Karimi, N. "On the effects of NH₃ addition to a reacting mixture of H₂/CH₄ under MILD combustion regime: Numerical modeling with a modified EDC combustion model," *Fuel* Vol. 326, 2022, p. 125096.
- [40] Mousavi, S. M., Kamali, R., Sotoudeh, F., Karimi, N., and Lee, B. J. "Numerical Investigation of the Plasma-Assisted MILD Combustion of a CH₄/H₂ Fuel Blend Under Various Working Conditions," *Journal of Energy Resources Technology* Vol. 143, No. 6, 2020.
- [41] Asadi, A., Kadijani, O. N., Doranehgard, M. H., Bozorg, M. V., Xiong, Q., Shadloo, M. S., and Li, L. K. B. "Numerical study on the application of biodiesel and bioethanol in a multiple injection diesel engine," *Renewable Energy* Vol. 150, 2020, pp. 1019-1029.
- [42] Hong, Z., Vasu, S. S., Davidson, D. F., and Hanson, R. K. "Experimental Study of the Rate of $\text{OH} + \text{HO}_2 \rightarrow \text{H}_2\text{O} + \text{O}_2$ at High Temperatures Using the Reverse Reaction," *The Journal of Physical Chemistry A* Vol. 114, No. 17, 2010, pp. 5520-5525.

- [43] Blocquet, M., Schoemaeker, C., Amedro, D., Herbinet, O., Battin-Leclerc, F., and Fittschen, C. "Quantification of OH and HO₂ radicals during the low-temperature oxidation of hydrocarbons by Fluorescence Assay by Gas Expansion technique," *Proceedings of the National Academy of Sciences* Vol. 110, No. 50, 2013, pp. 20014-20017.
- [44] El-Mahallawy, F., and Habik, S.-D. *Fundamentals and technology of combustion*: Elsevier, 2002.
- [45] Mousavi, S. M., Kamali, R., Sotoudeh, F., Karimi, N., and Jeung, I.-S. "Numerical Investigation of the Effects of Swirling Hot Co-Flow on MILD Combustion of a Hydrogen–Methane Blend," *Journal of Energy Resources Technology* Vol. 142, No. 11, 2020.

초 록

저선회 화염은 유동의 각운동량이 부족하여 와류를 분해하지 못하여 발생하는 원리를 갖는다. 대신에 연소실의 경계를 벗어나면서 유동이 발산하게 된다. 2가지의 막힘률과 2가지의 프랙탈 반복 횟수를 조합하여 만든 난류생성판을 사용하여 산업용 크기의 저선회 연소기에 대한 수치적 연구가 진행되었다. 본 연구에서는 압력 기반의 Navier-Stokes 방정식을 사용하여 3차원 대와류 난류 모델로서 Dynamic Smagorinsky를 적용하였다. 입구에서는 상압 조건의 메탄/공기 예혼합기가 당량비 0.49 로 유입되었고, 아격자 기반의 적응형 격자 세밀화 기법을 이용하여 관심영역에 정제된 격자를 얻어낼 수 있었다. 수치해석 결과에 대한 검증을 위해 연소기의 난류 강도를 나타내는 스윙수를 실험값과 비교하였고, 둘 사이의 오차는 0.9% 미만 이었다. 프랙탈 형상이 적용된 4개의 난류 생성판에 대해 연소와 연관된 주요 원인 중 하나인 난류강도를 확인하였다. 비반응 유동에서 난류강도, 유동 체류 시간, 와도, 그리고 속도구배 측면에서 73% 막힘률과 4번의 프랙탈 패턴 반복이 조합된 난류생성판이 가장 좋은 경우이고, 73% 막힘률과 3번의 프랙탈 패턴 반복이 조합된 난류생성판이 가장 나쁜 경우로 판단했다. 반응 유동을 통해서도 화염면과 반응영역에 대해 확인하였다. OH 라디칼을 통해 연소 효율이 가장 좋은 케이스에서 NO 배출 가스가 가장 낮음을 확인하였다.

주요어: 저선회 연소, 전산유체역학, 대와류모사, 적응형 격자 세밀화 기법, 난류 생성판, 프랙탈 형상

학 번: 2021-26314